Supporting information for the main manuscript:

”Strain budget of the Ecuador-Colombia subduction zone: a stochastic view”

B. Gombert[1], Z. Duputel[1], R. Jolivet [2], M. Simons[3], J. Jiang[4], C. Liang[5], E. Fielding[5], and L. Rivera[1]

[1] Institut de Physique du Globe de Strasbourg, UMR7516, Université de Strasbourg, EOST/CNRS
[2] Laboratoire de géologie, Département de Géosciences, École Normale Supérieure, PSL Research University, CNRS UMR, Paris, France
[3] Seismological Laboratory, Geological and Planetary Sciences, California Institute of Technology, Pasadena, California, USA
[4] Institute of Geophysics and Planetary Physics, University of California, San Diego, La Jolla, California, USA
[5] Jet Propulsion Laboratory, California Institute of Technology, Pasadena, California, USA

This electronic supplement is a collection of additional figures referenced in the main article. These figures were added to ensure the precision of the description of our method and results.

Supplementary text T1

Following Ye et al. (2014) and Nocquet et al. (2017), we compare waveforms of the 1942 earthquake recorded at the DBN station (De Bilt, Netherlands) with stochastic waveform predictions at the same station for the 2016 Pedernales slip distribution.

We compute displacement Green's functions for each subfault patch using the Kikuchi-Kanamori program (Kikuchi and Kanamori, 2003; Kikuchi, Masayuki and Kanamori, Hiroo, 1982). For comparison, we then convolve predicted stochastic waveforms with the instrumental response of the Galitzin seismometer that recorded the 1942 earthquake (pendulum and galvanometer periods T_p=T_g=25 s and gain factor V_m=310; Charlier and Van Gils, 1953).

In Fig. S10a, we first compare 1942 waveforms with predictions of the kinematic slip model (i.e., for the posterior distributions of slip, rise-times, rupture velocities) and hypocenter location obtained for the 2016 Pedernales earthquake. Model predictions show poor fit to the 1942 earthquake waveform. In Fig. S10b, we then compute predictions for the same kinematic slip distribution, but with a hypocenter location between the two slip asperities. With that hypocenter location, model predictions have a very good fit to the 1942 waveform. Finally, in Fig. S10c, we predict waveforms for a slip distribution on the megathrust interface, but updip of the actual 2016 rupture. Notice, that the dip is different due to the variation of the slab interface geometry with depth. We also correct the slip amplitude for the variation of shear modulus in our velocity model (cf., Fig. S2). Similarly to the previous case, the hypocenter is located between the two slip asperities. In this scenario, we are also able to explain the 1942 waveform. It illustrates that the teleseismic P-waveform is mostly sensitive to the relative location of the hypocenter and slip asperity rather than the absolute location of the earthquake.

Supplementary movie M1: Variability in the Ecuador-Colombia geodetic coupling solution The animation is made with 150 models randomly selected in the posterior population represented by the background colour. Grey lines are the 2 m contour intervals of 150 co-seismic models also randomly selected in the posterior population.

Supplementary movie M2: Temporal evolution of co-seismic slip of the 2016 Pedernales earthquake. (left) Posterior mean model of the cumulative slip. The bottom-right inset shows the stochastic source time function. **(right)** Incremental slip on the fault. The red star marks the inverted posterior mean hypocenter location.

Supplementary movie M3: Variability in the 2016 Pedernales earthquake co-seismic slip distribution solution The animation is made with 200 models randomly selected in the posterior population.

Table S1: InSAR observations used in this study.

Satellite	**Orbit**	**Acquisition dates**	**N° of data**	**Std.**	**Corr. length**
ALOS-2	ascending	07/02/16 - 01/05/16	130	5.3 mm	2.88 km
ALOS-2	descending	01/04/16 - 29/04/16	483	9.2 mm	11.90 km
Sentinel-1A	descending	12/04/16 - 24/04/16	380	5.0 mm	15.0 km

Table S2: Seismological data and filtering used in this study. We use a 4^{th} order Butterworth bandpass filter.

Station	Type	Filter corner frequencies		
		East	North	Up
bahi	HRGPS	0.015Hz - 0.08Hz	0.015Hz - 0.08Hz	0.015Hz - 0.08Hz
cabp	HRPGS	0.015Hz - 0.08Hz	0.015Hz - 0.08Hz	0.015Hz - 0.08Hz
ecec	HRPGS	0.015Hz - 0.08Hz	0.015Hz - 0.08Hz	0.015Hz - 0.08Hz
flfr	HRPGS	0.015Hz - 0.08Hz	0.015Hz - 0.08Hz	0.015Hz - 0.08Hz
mlec	HRPGS	0.015Hz - 0.08Hz	0.015Hz - 0.08Hz	0.015Hz - 0.08Hz
momp	HRPGS	0.015Hz - 0.08Hz	0.015Hz - 0.08Hz	0.015Hz - 0.08Hz
onec	HRPGS	0.015Hz - 0.08Hz	0.015Hz - 0.08Hz	0.015Hz - 0.08Hz
pdns	HRPGS	0.015Hz - 0.08Hz	0.015Hz - 0.08Hz	0.015Hz - 0.08Hz
ISPT	Strong motion	N/A	0.015Hz - 0.08Hz	0.015Hz - 0.08Hz
PDNS	Strong motion	0.037Hz - 0.08Hz	0.037Hz - 0.08Hz	0.015Hz - 0.08Hz
LGCB	Strong motion	0.015Hz - 0.08Hz	0.015Hz - 0.08Hz	0.015Hz - 0.08Hz
AATC	Strong motion	0.028Hz - 0.08Hz	0.028Hz - 0.08Hz	0.032Hz - 0.08Hz
AES1	Strong motion	N/A	N/A	0.015Hz - 0.08Hz
AMNT	Strong motion	N/A	0.015Hz - 0.08Hz	0.015Hz - 0.08Hz
APED	Strong motion	0.035Hz - 0.08Hz	0.035Hz - 0.08Hz	0.035Hz - 0.08Hz
ATON	Strong motion	0.015Hz - 0.08Hz	0.015Hz - 0.08Hz	0.015Hz - 0.08Hz
AV18	Strong motion	0.015Hz - 0.08Hz	0.015Hz - 0.08Hz	0.015Hz - 0.08Hz
AV21	Strong motion	0.032Hz - 0.08Hz	0.015Hz - 0.08Hz	0.015Hz - 0.08Hz

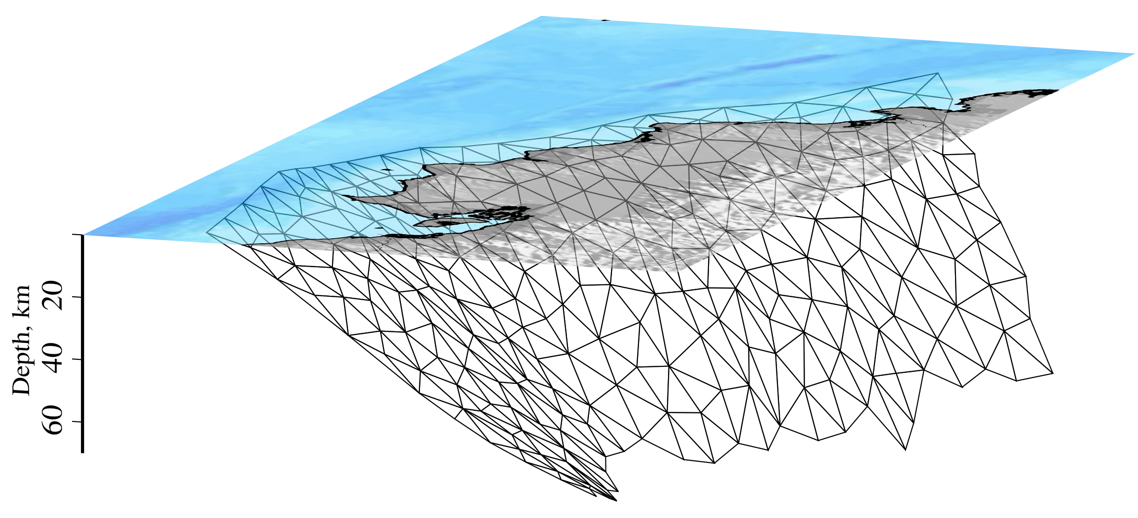

Figure S1: **Parametrization of the megathrust interface used for the coupling inversion.** Coupling value is inverted at each nodes

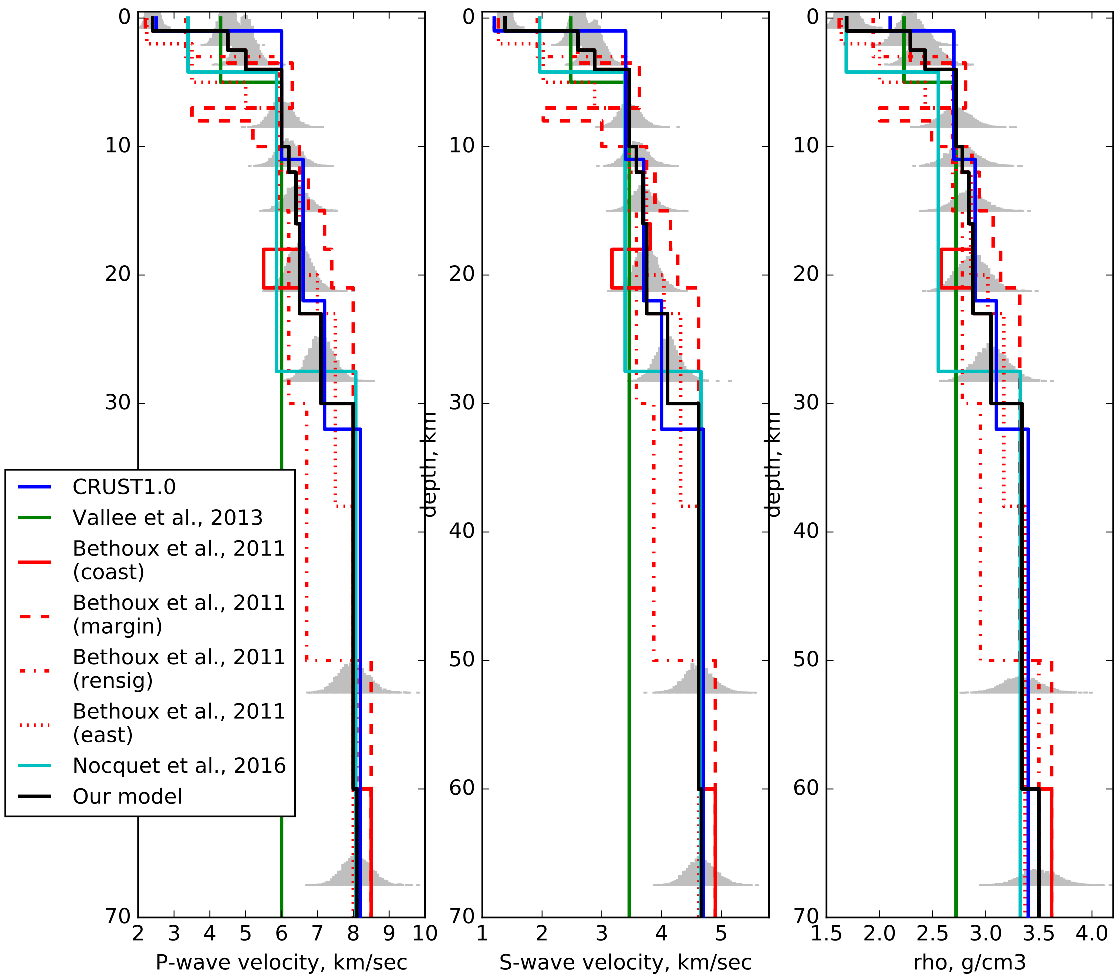

Figure S2: **Different models variability of the P-wave, S-wave, and density as a function of depth in central Ecuador.** A layered model used in this study for Green's function [GF] calculations is plotted as a solid black line. The blue line represents the CRUTST2.0 model in the area (`http://igppweb.ucsd.edu/~gabi/rem.html`). The other models are from (Vallee et al., 2013; Bethoux et al., 2011; Nocquet et al., 2017). Grey histograms are the probability density function representing our confidence level on the elastic properties, as used to build the model prediction error.

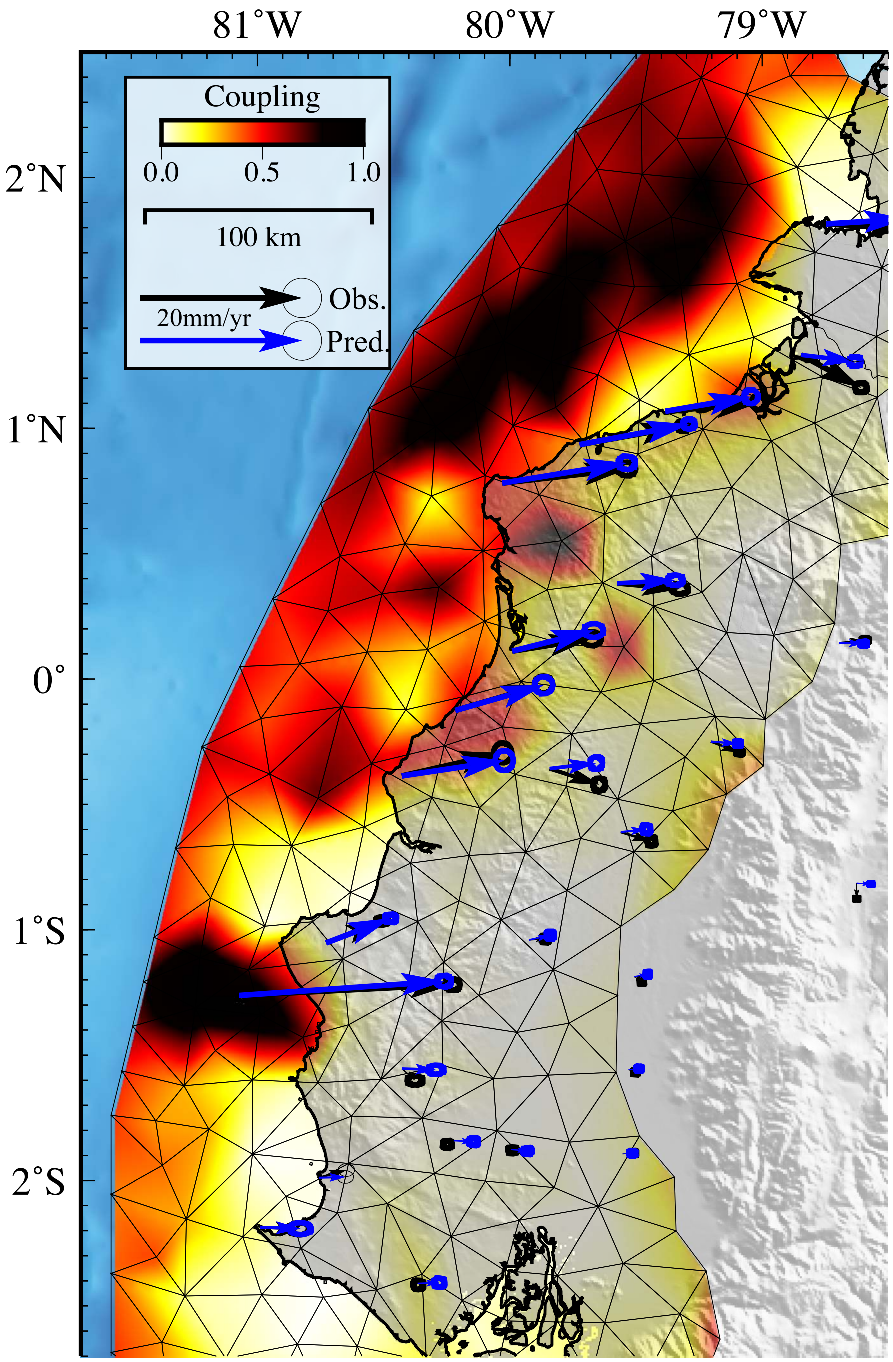

Figure S3: **Posterior Median coupling model.** Thin black lines represent the fault parametrization. Coupling values are inverted at each nodes. Interseismic GPS displacement and predictions for the median model are plotted as black and blue arrows, respectively.

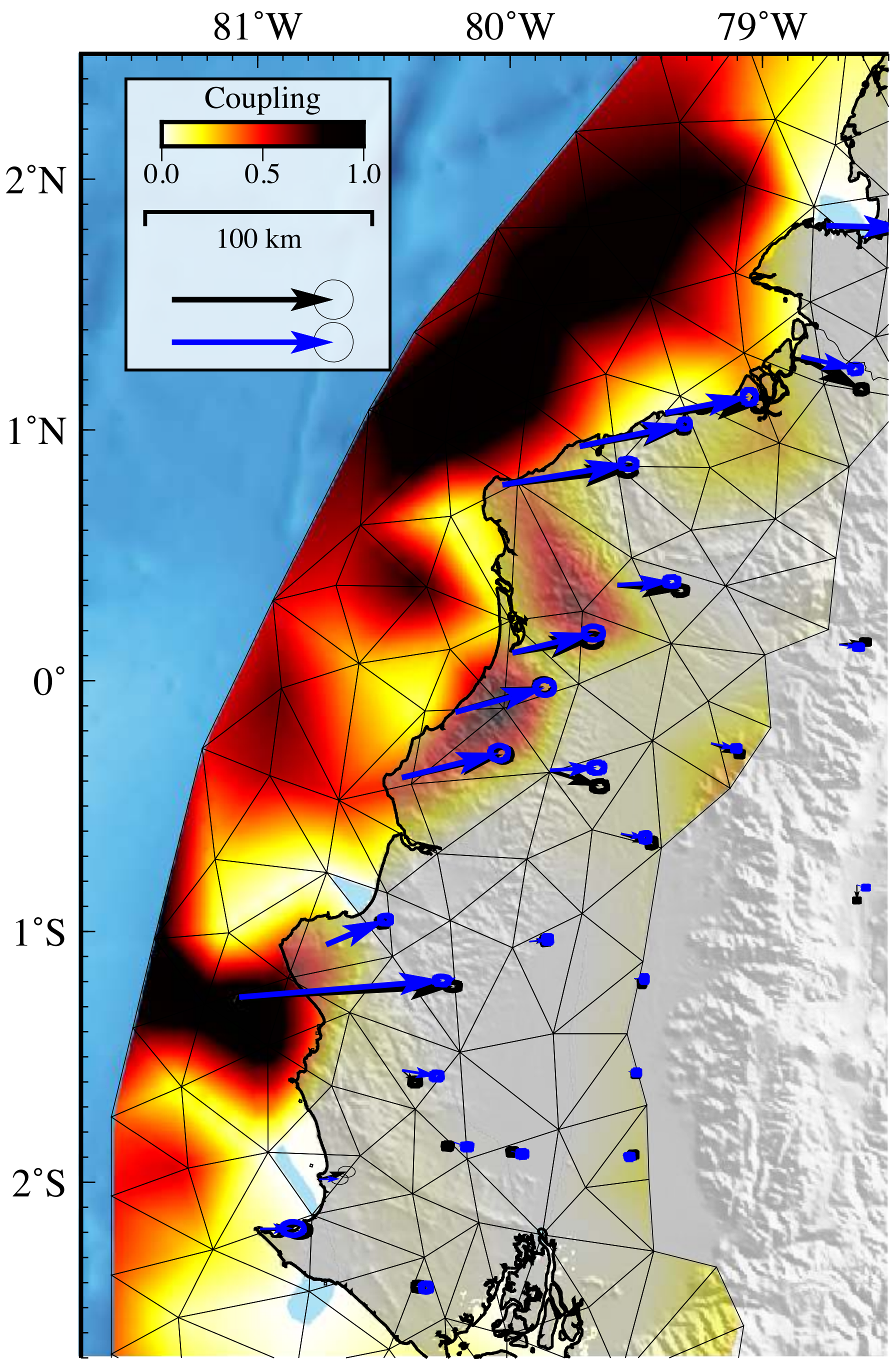

Figure S4: **Posterior Mean coupling model for a coarse parametrisation.** Same as Figure 2a. in the main text but obtained with a coarser fault parametrisation.

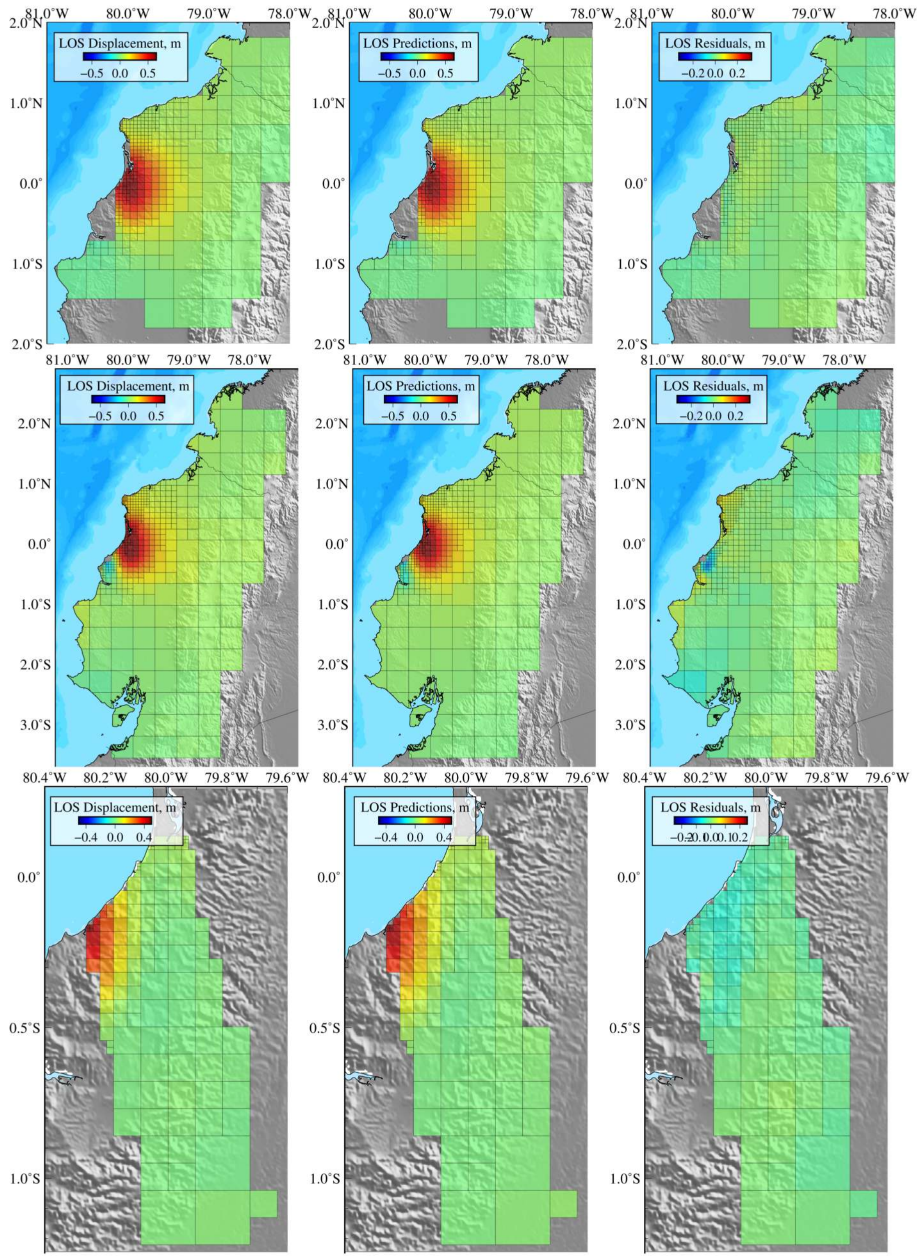

Figure S5: **Decimated InSAR observations, predictions, and residuals**. **(a, d, g)** Decimated InSAR observations inverted in this study. **(b, e, h)** Predictions for the posterior mean model. **(c, f, i)** Residuals of the Sentinel (top row), descending ALOS-2 (middle row), and ascending ALOS-2 (bottom row) interferograms.

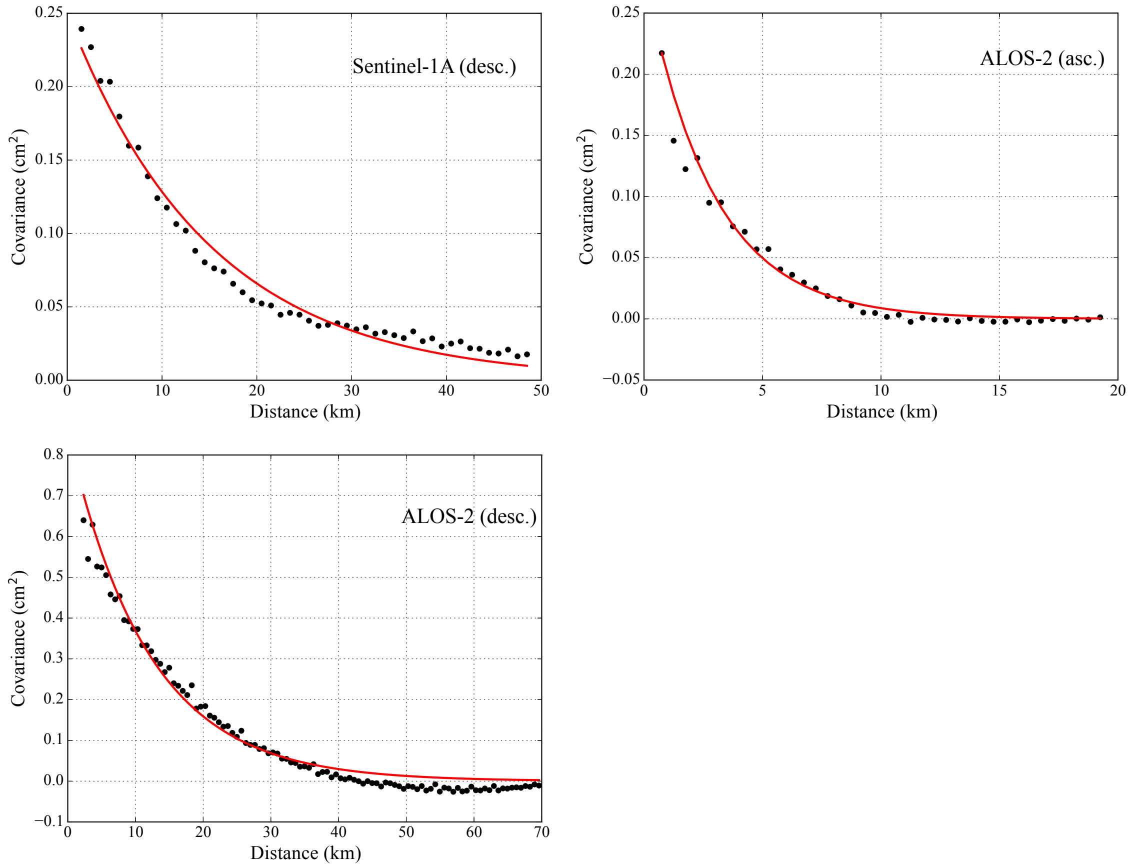

Figure S6: **Empirical covariance functions for the InSAR observations** 1D empirical covariance functions and the associated best-fit exponential function for each tracks. For each image, we compute the empirical covariance as a function of the distance between pixels and then fit an exponential function to these covariances (Jolivet et al., 2012). This exponential function is then used to build the data covariance matrix used in the inversion.

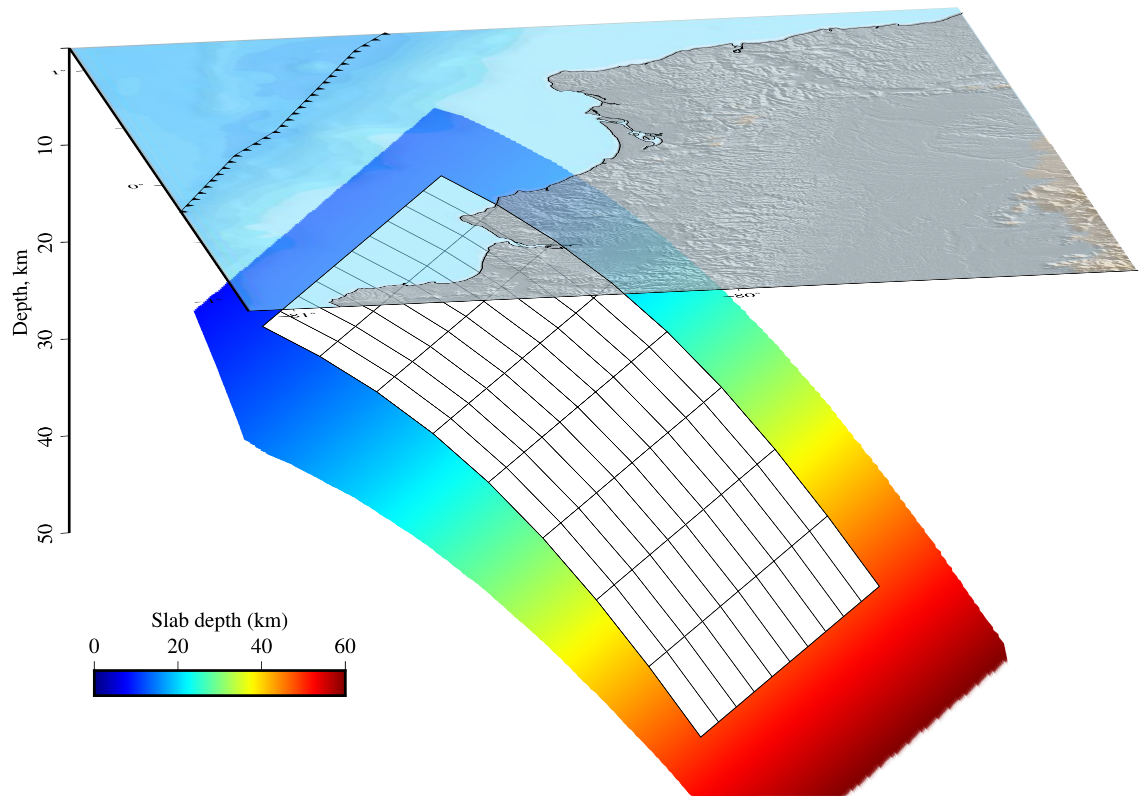

Figure S7: **Parametrization of the megathrust interface used for the co-seismic inversion** The coloured plane represent the slab1.0 model (Hayes et al., 2012). Each subfault patch is a 15 km x 15 km square

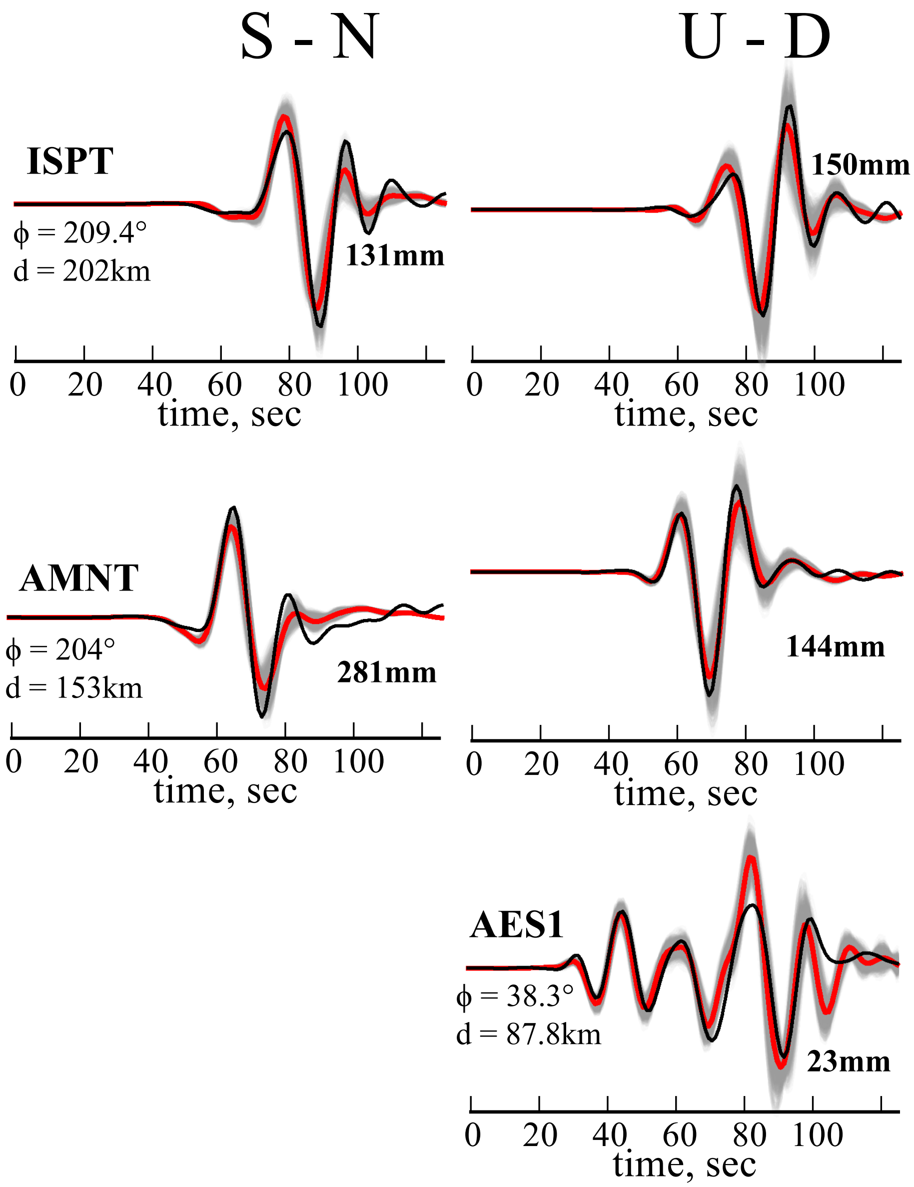

Figure S8: **Strong-motion observations and model predictions not presented in Figure 6 in the main text.** The North (left) and vertical (right) components of each station are plotted around the map. For each waveform, the bold number indicates it's maximum amplitude. The station azimuth Φ and distance d to the epicenter are also given. The black line is the recorded waveform. The gray lines are the stochastic predictions for our posterior model. The red line is the mean of the stochastic predictions.

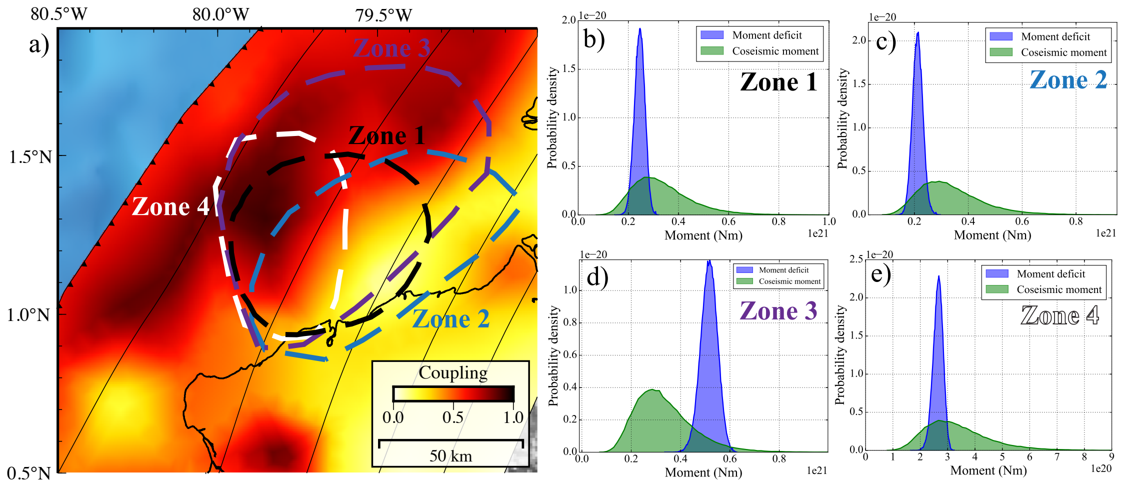

Figure S9: **Comparaison of co-seismic moment and moment deficit in the 1958 earthquake region. a)** The background colour represents the coupling posterior mean model. The black dashed lines delimit four different areas where the co-seismic moment of the 1958 event and moment deficit for the 1906 - 1958 period are computed. **b-e)** Probability densities of the co-seismic moment released by the 1958 earthquake and the moment deficit accumulated between 1906 and 1958 in the different dashed area shown in a).

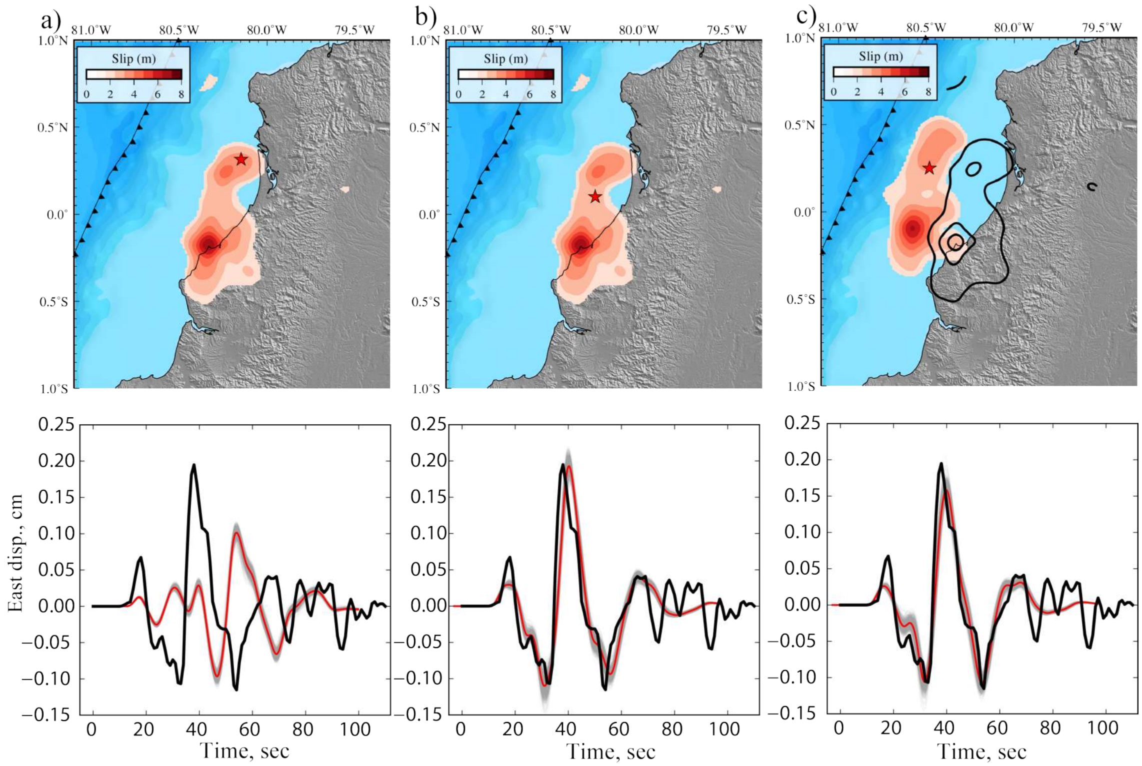

Figure S10: **Comparison of model predictions and 1942 earthquake waveform recorded in the DBN station, Netherlands. (top)** Slip model and hypocenter location (red star) used to compute the predictions shown in the bottom row. The model presented in a) results from the kinematic slip inversion of the 2016 earthquake. The models in b) and c) use a different hypocenter located between the two main slip asperities. The slip model in c) is the same as in a) and b), but located updip along the megathrust interface. Black lines in c) are slip contours of the original slip model. **(bottom)** East component waveform recorded at DBN for the 1942 earthquake (in black) and stochastic predictions (in grey) for the model shown on top. The red line is the posterior mean prediction. Predictions were convolved with the instrumental response of the Galitzin that recorded the event.

References

Bethoux, N., Segovia, M., Alvarez, V., Collot, J.-Y., Charvis, P., Gailler, A., and Monfret, T. (2011). Seismological study of the central Ecuadorian margin: Evidence of upper plate deformation. *Journal of South American Earth Sciences*, 31(1):139–152.

Charlier, C. and Van Gils, J. (1953). Liste des stations seismologiques mondiales. *Association internationale de seismologie, Observatoire Royal de Belgique*.

Hayes, G. P., Wald, D. J., and Johnson, R. L. (2012). Slab1. 0: A three-dimensional model of global subduction zone geometries. *Journal of Geophysical Research: Solid Earth*, 117(B1).

Jolivet, R., Lasserre, C., Doin, M.-P., Guillaso, S., Peltzer, G., Dailu, R., Sun, J., Shen, Z.-K., and Xu, X. (2012). Shallow creep on the Haiyuan fault (Gansu, China) revealed by SAR interferometry. *Journal of Geophysical Research: Solid Earth*, 117(B6).

Kikuchi, M. and Kanamori, H. (2003). *Note on Teleseismic Body-Wave Inversion Program*. `http://www.eri.u-tokyo.ac.jp/ETAL/KIKUCHI/`.

Kikuchi, Masayuki and Kanamori, Hiroo (1982). Inversion of complex body waves. *Bulletin of the Seismological Society of America*, 72(2):491–506.

Nocquet, J.-M., Jarrin, P., Vallée, M., Mothes, P., Grandin, R., Rolandone, F., Delouis, B., Yepes, H., Font, Y., Fuentes, D., et al. (2017). Supercycle at the Ecuadorian subduction zone revealed after the 2016 Pedernales earthquake. *Nature Geoscience*, 10(2):145–149.

Vallee, M., Nocquet, J.-M., Battaglia, J., Font, Y., Segovia, M., Regnier, M., Mothes, P., Jarrin, P., Cisneros, D., Vaca, S., et al. (2013). Intense interface seismicity triggered by a shallow slow slip event in the Central Ecuador subduction zone. *Journal of Geophysical Research: Solid Earth*, 118(6):2965–2981.

Ye, L., Lay, T., Koper, K. D., Smalley Jr., R., Rivera, L., Bevis, M. G., Zakrajsek, A. F., and Teferle, F. N. (2014). Complementary slip distributions of the August 4, 2003 Mw 7.6 and November 17, 2013 Mw 7.8 South Scotia Ridge earthquakes. *Earth Planet. Sci. Lett.*, 401:215–226.